Coupled oscillations of vortex cores confined in a ferromagnetic elliptical disk

Hiroshi Hata* and Minori Goto
Department of Physics, Keio University, 3-14-1 Hiyoshi, Yokohama, Kanagawa 223-8522, Japan

Akinobu Yamaguchi†
Laboratory of Advanced Science and Technology for Industry, University of Hyogo, 3-1-2 Koto, Kamigori-cho, Ako-gun, Hyogo 678-1205, Japan

Tomonori Sato and Yoshinobu Nakatani
Graduate School of Informatics and Engineering, University of Electro-Communications, 1-5-1 Chofugaoka, Chofu, Tokyo 182-8585, Japan

Yukio Nozaki‡
Department of Physics, Keio University, 3-14-1 Hiyoshi, Yokohama, Kanagawa 223-8522, Japan and JST, CREST, 5, Sanbancho, Chiyoda-ku, Tokyo 102-0075, Japan

(Received 27 December 2013; revised manuscript received 31 July 2014; published 22 September 2014)

By solving the Thiele equation with simultaneous application of a radio-frequency (rf) magnetic field ($\boldsymbol{h}_{\mathrm{rf}}$) and an rf spin current ($\boldsymbol{j}_{\mathrm{sp}}$), the dynamic susceptibility of exchange-coupled vortices in response to $\boldsymbol{h}_{\mathrm{rf}}$ and $\boldsymbol{j}_{\mathrm{sp}}$ was obtained. It was found that the four eigenmodes expected for two vortices trapped in a magnetic elliptical disk were coupled to different components of $\boldsymbol{h}_{\mathrm{rf}}$ and $\boldsymbol{j}_{\mathrm{sp}}$. As a consequence, orthogonal $\boldsymbol{h}_{\mathrm{rf}}$ and $\boldsymbol{j}_{\mathrm{sp}}$ (which are simultaneously generated by the application of an rf current to an elliptical disk) can excite two modes with different eigenfrequencies. This result suggests that a fieldlike nonadiabatic torque caused by an rf spin current can be spectroscopically distinguished from the one caused by the rf magnetic field.

DOI: 10.1103/PhysRevB.90.104418 PACS number(s): 75.78.−n, 75.78.Cd, 75.78.Fg, 75.70.Kw

I. INTRODUCTION

To understand the dynamics of spins and also to discover their potential applications for spintronic devices, the magnetization dynamics in artificial micrometer- and nanometer-scale magnets have been studied extensively. The spin-transfer torque (STT) is a particularly interesting phenomenon because it is capable of switching the magnetization, making it a promising candidate for applications in nonvolatile magnetic memories [1–3]. The STT can also displace magnetic domain walls (DWs) in ferromagnetic wires [4,5]. When an electric current flows through a DW, the spin angular momentum of the conduction electrons is transferred to the local magnetization both adiabatically and nonadiabatically [6,7]. Consequently, the STT is exerted on the local magnetization within the DWs, and its strength depends upon the DW's magnetic structure. However, note that the Oersted field caused by the current flowing through the wire also affects the spin dynamics [8–10]. To quantify the relationship between the STT and the magnetic structure, it is important to individually evaluate the effects due to the STT and those due to the Oersted field.

In this study, we solve the Thiele equation considering both the radio-frequency (rf) Oersted fields and the rf spin torques in order to study the motion of two magnetic solitons (i.e., magnetic vortices) confined in an elliptical-shaped ferromagnetic disk [Fig. 1(a)]. The magnetic vortex is an in-plane continuous swirling closure magnetization structure with a tiny central core that is magnetized perpendicular to the plane [11,12]. The states of a pair of vortices are characterized by two Boolean parameters: the polarity p_j and the chirality c_j, where $j = 1,2$ is the index of each vortex. The polarity p_j describes whether the out-of-plane component at the core points up ($p_j = +1$) or down ($p_j = -1$). The chirality c_j describes whether the in-plane curling direction is clockwise ($c_j = +1$) or counterclockwise ($c_j = -1$). In the case of two vortices confined to an elliptical disk, the vortices have opposite chirality ($c_1 = -c_2$) in order to decrease the exchange energy of the disk.

There have been several reports on vortex-vortex interactions in laterally [13–19] and longitudinally [20,21] separated disks. Studies on vortex pairs confined to a single disk are reported in Refs. [22] and [23]. It is known that magnetic interactions among vortices can remove the degeneracy of the gyration modes in the two vortices with different combinations of p_j and c_j. The dynamic susceptibility of magnetostatically coupled vortices has been analytically studied by Shibata *et al.* [13] (using a rigid vortex model) and Sukhostavets *et al.* [14] (using a two-vortex model). In such systems, the presence of the eigenmodes of the center-mass motion and the relative motion of the vortex cores was theoretically predicted [21,23]. An exchange interaction among vortices can also remove the degeneracy. The dynamical properties of exchange-coupled vortices in the same ferromagnetic disk have been investigated by Buchanan *et al.* [22]. They observed an rf-field induced resonance spectrum of two exchange-coupled vortices using a vector network analyzer to measure ferromagnetic resonance. The eigenmodes that appeared in the exchange-coupled vortices were consistent with those expected from a phenomenological calculation and corresponding micromagnetic simulations. It was noted that a

*Present address: Institute for Chemical Research, Kyoto University, Gokasho, Uji, Kyoto 611-0011, Japan.
†Corresponding author: yamaguti@lasti.u-hyogo.ac.jp
‡Corresponding author: nozaki@phys.keio.ac.jp

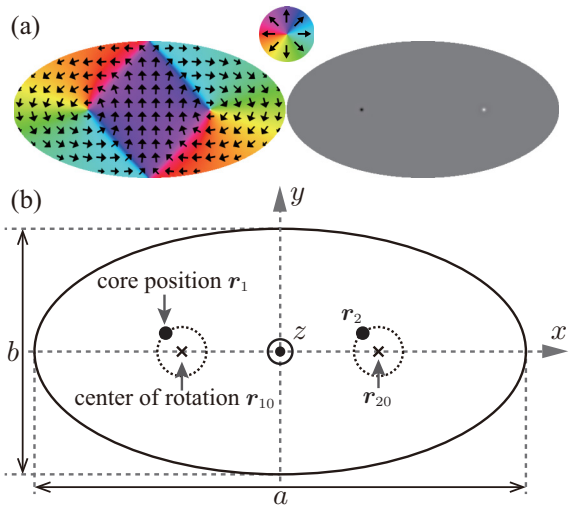

FIG. 1. (Color online) A pair of vortices confined in an elliptical disk. (a) Micromagnetic simulation of the magnetization distribution. Left: Colors represent the in-plane magnetization direction. Right: Black and white represent downward and upward out-of-plane magnetization, respectively. Gray denotes regions with no out-of-plane magnetization component (in-plane magnetization component only). (b) The coordinate system used in this study. The origin of the coordinate system is placed at the center of the elliptical disk.

deformation of the closure domain during the gyration plays an important role in the dynamic susceptibility of vortices confined in the same disk. The temporal variation in the magnetic energy caused by the deformation of the closure domain depends on the phase difference in the translational modes of the exchange-coupled vortices. Although these modes have been well studied when excited by an rf field, the dynamic susceptibility with respect to an rf current (which is significant for evaluating the spin-transfer torque) has not yet been sufficiently researched. Furthermore, only three of the four theoretically expected eigenmodes have been observed under the influence of an rf magnetic field. In this study, the dynamic susceptibility of exchange-coupled vortices with respect to the simultaneous application of $\boldsymbol{h}_{\rm rf}$ and $\boldsymbol{j}_{\rm sp}$ was analytically studied by solving the Thiele equation. From the analytical calculation, it was found that degeneracy in the translational modes excited by $\boldsymbol{h}_{\rm rf}$ and $\boldsymbol{j}_{\rm sp}$ could be removed by using the vortices trapped in the isolated elliptical disk, unlike in the cases of a single vortex or magnetostatically coupled vortices. That is to say, the contributions of the rf current and the rf magnetic field to dynamic susceptibility can be separately examined. We also found that all of the theoretically expected four eigenmodes can be realized by using both the rf magnetic field and the rf current. The precise formulation of the core motions induced by $\boldsymbol{h}_{\rm rf}$ and $\boldsymbol{j}_{\rm sp}$ and the method used to evaluate the nonadiabaticity parameter of STT will be presented in this paper.

This paper is organized as follows. In Sec. II, the analytical model we used to solve this problem is explained. In Sec. III, the magnetostatic energy that determines the restoring force of the vortices is discussed. In Sec. IV, the solutions of the Thiele equation are derived, and each eigenmode is explained. A comparison between the analytical calculation and the micromagnetic simulation is described in Sec. V; we also propose a method to experimentally examine the β term using a vortex pair. Finally, our study is summarized in Sec. VI.

II. ANALYTICAL MODEL

A. Coordinate system

The coordinate system used in this study is schematically shown in Fig. 1(b). The lateral dimensions of the ellipse are $a \times b$, and the thickness is L. The origin of the coordinate system is at the center of the disk. The position of each vortex core is described by $\boldsymbol{r}_j = (x_j, y_j)$, where j is the index number of the core. The center-of-mass coordinate, $\boldsymbol{r}_{\rm cm} \equiv (\boldsymbol{r}_1 + \boldsymbol{r}_2)/2$, and the relative coordinate, $\boldsymbol{r}_{\rm rel} \equiv \boldsymbol{r}_2 - \boldsymbol{r}_1$, are also used. An rf electric current (namely the rf spin current, $\boldsymbol{j}_{\rm sp}$) or rf magnetic field ($\boldsymbol{h}_{\rm rf}$) is applied in arbitrary in-plane directions. $\boldsymbol{j}_{\rm sp}$ or $\boldsymbol{h}_{\rm rf}$ will excite the rotational motion of the vortex cores at its eigenfrequency. The rotational motion of each core can be expressed in the following equation:

$$\begin{pmatrix} x_j \\ y_j \end{pmatrix} = \begin{pmatrix} x_{j0} + X_j e^{i\omega t} \\ Y_j e^{i\omega t} \end{pmatrix}, \tag{1}$$

where ω is the angular frequency, x_{j0} is the equilibrium position, and X_j and Y_j are the complex amplitudes of core rotation. The amplitudes in real space are given by

$$\begin{aligned} {\rm Re}[X_j e^{i\omega t}] &= {\rm Re}[X_j]\cos\omega t - {\rm Im}[X_j]\sin\omega t, \\ {\rm Re}[Y_j e^{i\omega t}] &= {\rm Re}[Y_j]\cos\omega t - {\rm Im}[Y_j]\sin\omega t. \end{aligned} \tag{2}$$

B. Thiele equation

The motion of each vortex core in the x-y plane can be described by the Thiele equation [24,25] including spin torque terms [6,7,26–29]:

$$\boldsymbol{G}(p_j) \times (\boldsymbol{u} - \dot{\boldsymbol{r}}_j) = -\frac{\delta U(\boldsymbol{r}_1, \boldsymbol{r}_2)}{\delta \boldsymbol{r}_j} - \alpha D \dot{\boldsymbol{r}}_j + \beta D \boldsymbol{u}. \tag{3}$$

The first term on the left-hand side of Eq. (3) consists of the adiabatic spin-transfer torque and the gyroforce. Here, the gyrovector $\boldsymbol{G}(p_j)$ is given by

$$\boldsymbol{G}(p_j) = -\frac{2\pi L M_s}{\gamma} p_j \hat{\boldsymbol{z}} = -G_0 p_j \hat{\boldsymbol{z}}, \tag{4}$$

where M_s and γ are the saturation magnetization and the gyromagnetic ratio, respectively. The velocity vector $\boldsymbol{u}$, associated with the spin transfer torque from spin current $\boldsymbol{j}_{\rm sp}$, can be described by

$$\boldsymbol{u} = e^{i\omega t}\left(\frac{\mu_{\rm B} P}{q_e M_s} j_x, \frac{\mu_{\rm B} P}{q_e M_s} j_y\right) \equiv e^{i\omega t}(u_x, u_y), \tag{5}$$

where $\mu_{\rm B}$, P, and q_e denote the Bohr magneton, spin polarization, and electron charge, respectively. j_x and j_y are the x and y components of the electric current density, respectively.

The terms on the right-hand side of Eq. (3) are described as follows. The first term on the right-hand side of Eq. (3) is the restoring force attributed to the magnetic potential $U(\boldsymbol{r}_1, \boldsymbol{r}_2)$. In general, the magnetic potential consists of the magnetostatic energy, exchange energy, Zeeman energy, and

anisotropy energy. However, the force associated with exchange energy is negligible compared with that associated with the magnetostatic energy in the micron-scale disk [10]. The magnetocrystalline anisotropy energy is ignored in this study because a soft magnetic material, permalloy, is generally used to study the dynamics of a magnetic vortex. Thus, the magnetic potential can be written as $U = U_m + U_z$, where U_m and U_z indicate the magnetostatic energy and the Zeeman energy, respectively. The magnetostatic energy can be expressed in the center-of-mass and relative frames simultaneously by the following:

$$U_m = \frac{\kappa_x}{2}x_{cm}^2 + \frac{\kappa_y}{2}y_{cm}^2 + \frac{\mu}{4}(x_{rel} - b)^2 + \frac{\mu}{4}y_{rel}^2, \qquad (6)$$

where κ_x and κ_y correspond to the stiffness constant of the vortex along the x and y axes in the center-of-mass frame, respectively, and μ corresponds to the stiffness constant in the relative frame. The detailed derivation of Eq. (6) is shown in Sec. III.

Herein, we will discuss the Zeeman energy of two vortices in an isolated elliptical disk. If the core displacement caused by an external magnetic field is much smaller than the inter-core distance, and the rotational amplitude of each core is sufficiently small, it is reasonable to assume that the Zeeman energy for the vortices in the elliptical disk is given by a linear combination of the Zeeman energy for the two isolated vortices. The Zeeman energy of a vortex formed in a circular disk is given by $U_{z,single} = cl(\hat{z} \times \boldsymbol{H}_{ext}) \cdot \boldsymbol{r}$, where $l \equiv \pi\xi M_s LR$, $\xi = 2/3$ for a "side-charge-free" model, R is the disk radius (namely, the radius of the vortex structure), and $\boldsymbol{r}$ is the position of the vortex core [30]. As a consequence, the Zeeman energy for vortices in the elliptical disk is given by

$$U_z = c_1 l(\hat{z} \times \boldsymbol{H}_{ext}) \cdot \boldsymbol{r}_1 + c_2 l(\hat{z} \times \boldsymbol{H}_{ext}) \cdot \boldsymbol{r}_2. \qquad (7)$$

In this paper, we consider the rf magnetic field as the only external magnetic field: $\boldsymbol{H}_{ext} = \boldsymbol{h}_{rf} = e^{i\omega t}(h_x, h_y)$, where $h_{x(y)}$ is the amplitude of the rf field.

The second term on the right-hand side of Eq. (3) is the damping force, with α being the Gilbert damping constant and D the diagonal element of the damping tensor. The third term on the right-hand side of Eq. (3) is the nonadiabatic spin transfer torque. Here, β is the nonadiabaticity parameter.

III. MAGNETOSTATIC ENERGY

In this section, the magnetostatic energy of the vortex pair is discussed. The changes in the magnetostatic energy because of the applications of the magnetic field along the y and x axes are calculated in Secs. III A and III B, respectively. The validity of the expressions derived in Secs. III A and III B is confirmed by micromagnetic simulation in Sec. III C. The magnetostatic energies in the relative and center-of-mass frames are summarized in Sec. III D.

A. Two cores moving along the x direction

If the elliptical disk has two vortices, a diamond-shaped magnetic domain appears at the center of the disk as shown in Fig. 1(a). Figure 2(a) shows a schematic of the spin orientation in the elliptical disk. 90° domain walls are formed at line segments AB, BC, CD, and DA in Fig. 2(a). If magnetic poles

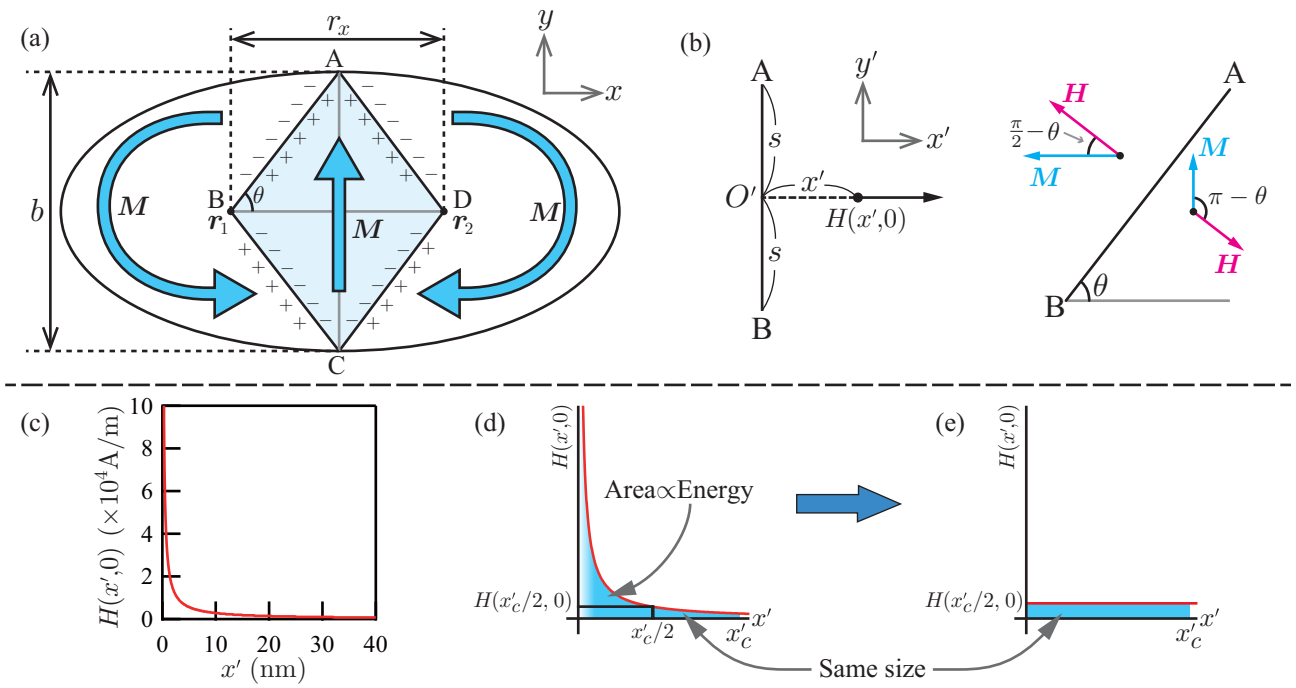

FIG. 2. (Color online) (a) Schematic of magnetic moment distribution. A diamond-shaped magnetic domain (i.e., quadrilateral ABCD) appears at the center of the disk. Line segments AB, BC, CD, and DA correspond to 90° domain walls. (b) The coordinate system for the magnetic field calculation and the coordinate model for the magnetostatic energy in the line segment AB. (c) Numerically calculated values of the magnetic field $H(x',0)$ as a function of x' at $\theta = 44.7°$. (d) Integration area to calculate the magnetostatic energy from the magnetic-field distribution. The integration area shown in (d) is simplified to (e).

appear at the domain walls, the magnetostatic energy will increase near the walls. Now, we calculate the magnetostatic energy as a function of the distance between the two cores along the x axis, r_x. As shown in Fig. 2(a), we define the angle between AB and BD as θ. We assume that points B and D move along the x axis, and that points A and C are fixed. The angle θ has a relationship with r_x given by the following:

$$\sin\theta = \frac{b}{\sqrt{b^2 + r_x^2}}, \quad \cos\theta = \frac{r_x}{\sqrt{b^2 + r_x^2}}. \tag{8}$$

First, we calculate the magnetostatic energy near the wall AB. The magnetic charge density on the wall AB can be described as

$$q = M_s(\cos\theta - \sin\theta). \tag{9}$$

If θ deviates from 45°, q is no longer zero. Next, the magnetic field $\boldsymbol{H}$ caused by q will be evaluated. We set the x',y' coordinate system, as shown in Fig. 2(b). The origin O' of the $x'y'$ system is set at the midpoint of the wall AB. By assuming a uniform distribution of the magnetic pole on the wall AB, $H(x',0)$ can be calculated as

$$H(x',0) = \frac{\lambda s}{2\pi\mu_0 x'} \frac{1}{(x'^2 + s^2)^{1/2}}, \tag{10}$$

where λ is the line density of the magnetic pole given by Lq, and $2s$ is the length of the wall AB, given by $b/2\sin\theta$. The numerically calculated values of the magnetic field $H(x',0)$ as a function of x at $\theta = 44.7°$ are shown in Fig. 2(c) [31]. Parameters used in numerical calculation in this study are summarized in Table I. The strength of $H(x',0)$ rapidly decreases with increasing x' and becomes less than 1×10^3 A/m at $x' = 28$ nm. Next, we calculate the magnetostatic energy caused by the magnetic pole. If x' is much smaller than the length of the wall AB, the effect of the magnetic pole around both ends can be ignored. Thus $H(x',y')$ can be written as a single variable, $H(x')$. In order to calculate the magnetostatic energy, we consider the energy of a small volume $2sLdx'$, and then integrate it from $x' = 0$ to $x' = \infty$,

$$U_{\mathrm{m,AB}} = -2sL\int_0^\infty M_s H(x')\left[\cos(\pi - \theta) + \cos\left(\frac{\pi}{2} - \theta\right)\right]dx'. \tag{11}$$

The integral in Eq. (11) corresponds to the (blue) shaded area in Fig. 2(d). However, this integral cannot be calculated because it goes to ∞ as x' goes to 0. Thus we terminate the calculation at the point x_c', where $H(x')$ becomes less than 1×10^3 A/m, and regard the size of the (blue) shaded areas in Figs. 2(d) and 2(e) as being the same, assuming that the magnetic field $H(x_c'/2)$ is uniformly distributed. x_c' is treated as a variable. The magnetostatic energy shown in Fig. 2(e) is given by

$$\begin{aligned} U_{\mathrm{m,AB}} &= -2sLM_s H\left(\frac{x_c'}{2}\right)x_c'\left[\cos(\pi - \theta) + \cos\left(\frac{\pi}{2} - \theta\right)\right] \\ &= \frac{M_s^2 b^2 L^2}{8\pi\mu_0}\left(1 - \frac{\cos\theta}{\sin\theta}\right)^2 \frac{1}{\sqrt{\frac{x_c'^2}{4} + s^2}}. \end{aligned} \tag{12}$$

Summing up the magnetostatic energies near the other walls, and changing the variable θ to r_x using Eq. (8), the total magnetostatic energy can be calculated as

$$U_m(r_x) = \frac{2M_s^2 L^2}{\pi\mu_0}(b - r_x)^2 \frac{1}{\sqrt{4x_c'^2 + b^2 + r_x^2}}. \tag{13}$$

To simplify $\sqrt{4x_c'^2 + b^2 + r_x^2}$ in Eq. (13), we carry out the following approximation. In the case of an elliptical disk with a diameter on the order of a μm, b and r_x on the order of a few μm, and x_c' on the order of tens of nm [Fig. 2(c)], we can neglect the variable $x_c'^2$. Next, assuming that the gyration radii of the vortex cores are measured in tens of nm, r_x can be approximated by b. Consequently, $\sqrt{4x_c'^2 + b^2 + r_x^2} \simeq \sqrt{2}b$. Equation (13) can be simplified as

$$\begin{aligned} U_m(r_x) &= \frac{\sqrt{2}M_s^2 L^2}{\pi\mu_0 b}(r_x - b)^2 \\ &= \frac{\mu}{4}(r_x - b)^2 = \frac{\mu}{4}(x_2 - x_1 - b)^2, \end{aligned} \tag{14}$$

where

$$\mu \equiv \frac{4\sqrt{2}M_s^2 L^2}{\pi\mu_0 b}. \tag{15}$$

The 4 in the denominator of Eq. (14) is introduced for convenience in subsequent calculations. As shown in Eq. (14), the magnetostatic energy can be expressed as that of a harmonic oscillator. Equation (14) simultaneously shows that the equilibrium position of each core is $x_{10} = -b/2$ and $x_{20} = b/2$.

TABLE I. Parameters used in numerical calculation and micromagnetic simulation. Material parameters are assumed to be permalloy ($Fe_{19}Ni_{81}$).

Physical quantity	Symbol	Value
Disk dimensions		
Length of major axis	a	2 μm
Length of minor axis	b	1 μm
Thickness	L	30 nm
Material parameters		
Saturation magnetization	M_s	1.0 Wb/m^2
Exchange stiffness constant	A	1.0×10^{-11} J/m
Gyromagnetic ratio	γ	2.2×10^5 m/As
Spin polarization	P	0.7
Gilbert damping constant	α	0.01
Nonadiabaticity parameter	β	0.01
External driving		
Current density	$j_{x(y)}$	1.0×10^{10} A/m^2
rf field	$h_{x(y)}$	7.96 A/m

B. Two cores moving along the y direction

When two cores move in the y direction (as schematically shown in Fig. 3), the lengths of the AB and BC walls are no longer the same. Here, the lengths of AB and BC are defined as $2s_1$ and $2s_2$, respectively. The distance between the two cores in the y direction is r_y, and the distance between the two cores along the x axis is fixed at b. We set $\angle\mathrm{ABE} = \theta_1$, $\angle\mathrm{EBC} = \theta_2$.

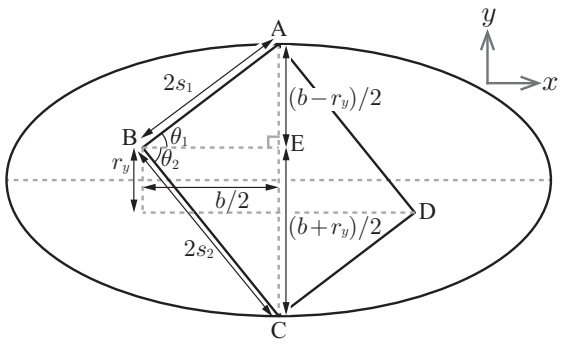

FIG. 3. Schematic geometry of domain walls in the elliptical disk when two cores move individually along the $+y$ and $-y$ directions.

We can calculate the magnetostatic energy in the same way as described in Sec. III A. The result is given by the following:

$$U_m(r_y) = 2 \times \frac{2\lambda_1 s_1^2 M_s L(\cos\theta_1 - \sin\theta_1)}{\pi\mu_0} \frac{1}{\sqrt{x^2+s_1^2}} + 2 \times \frac{2\lambda_2 s_2^2 M_s L(\cos\theta_2 - \sin\theta_2)}{\pi\mu_0} \frac{1}{\sqrt{x^2+s_2^2}} \simeq \frac{\sqrt{2}M_s^2 L^2}{\pi\mu_0 b} r_y^2 = \frac{\mu}{4} r_y^2 = \frac{\mu}{4}(y_2 - y_1)^2. \quad (16)$$

C. Comparison with micromagnetic simulation

To confirm the validity of the analytical form of the magnetostatic energy given by Eqs. (14) and (16), we performed a micromagnetic simulation. The object oriented micromagnetic framework (OOMMF) [32] was used for simulations that numerically integrate the Landau-Lifshitz-Gilbert (LLG) equation. First, a 2 μm $\times$ 1 μm $\times$ 30 nm elliptical disk was discretized into a numerical grid of 5 nm $\times$ 5 nm $\times$ 30 nm. The simulation parameters are summarized in Table I. As the Gilbert damping constant α does not depend on the static state, $\alpha = 1$ was used in this simulation to make it run faster. We set the two vortices to have $c_1 = -1$, $c_2 = 1$, and $p_1 = p_2 = -1$. Vortex cores are moved along the x and y axes by static magnetic fields, H_y and H_x. We calculated the r_x and r_y dependencies of the magnetostatic energy. Figures 4(a) and

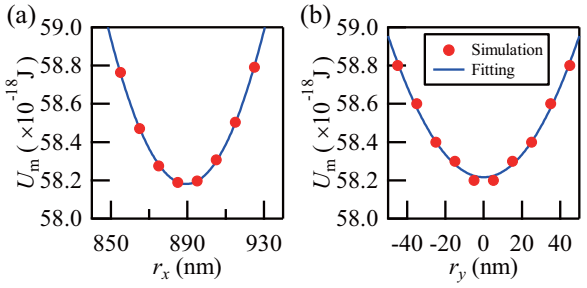

FIG. 4. (Color online) Micromagnetic simulation calculating the magnetostatic energy as a function of (a) r_x and (b) r_y. Solid circles and lines indicate values estimated by the simulation results and the fitting curves, respectively.

TABLE II. Fitting parameters.

	K_0	K_1	K_2
x	4.44×10^{-16} J	-8.67×10^{-10} J/m	4.88×10^{-4} J/m^2
y	5.82×10^{-17} J	-1.90×10^{-25} J/m	2.95×10^{-4} J/m^2

4(b) show the numerically evaluated magnetostatic energy as a function of r_x and r_y, respectively. A parabolic relationship between the magnetostatic energy and the distance between the two cores is clearly observed in both cases. In order to evaluate the effective stiffness constant, we fit the curve as quadratic function; $U_m(r_{x(y)}) = K_0 + K_1 r_{x(y)} + K_2 r_{x(y)}^2$. The result is summarized in Table II. We define $\mu_{\mathrm{sim},x} = 4K_{2(x)} = 1.952 \times 10^{-3}$ J/m^2 and $\mu_{\mathrm{sim},y} = 4K_{2(y)} = 1.180 \times 10^{-3}$ J/m^2, which correspond to the simulation result of μ in Eqs. (14) and (16), respectively. In contrast, the value of μ calculated using Eq. (15) is 1.290×10^{-3} J/m^2. The simulated $\mu_{\mathrm{sim},x}$ and $\mu_{\mathrm{sim},y}$ approximately coincide with the analytical μ. Consequently, we can confirm the validity of the magnetostatic energy in the relative coordinate.

D. Analytical expression of magnetostatic energy

In the zeroth-order approximation, the magnetostatic energy of the elliptical disk consisting of two vortices located at (x_1, y_1) and (x_2, y_2) is given by

$$U_{\mathrm{m}}(r_x, r_y) \simeq U_m(r_x) + U_m(r_y) = \frac{\mu}{4}(x_{\mathrm{rel}} - b)^2 + \frac{\mu}{4} y_{\mathrm{rel}}^2, \quad (17)$$

where x_{rel} and y_{rel} are the x and y components, respectively, of the relative position $\boldsymbol{r}_{\mathrm{rel}}$. If the distance between the two cores does not change during the gyration, the magnetostatic energy should be described in center-of-mass coordinates, where the movement of two cores can be interpreted as the movement of a single core at the barycenter. Note that the magnetostatic energy of the center-of-mass coordinate is similar to that of the single vortex state given by

$$U_{\mathrm{m}} = \frac{\kappa_x}{2} x_{\mathrm{cm}}^2 + \frac{\kappa_y}{2} y_{\mathrm{cm}}^2, \quad (18)$$

where x_{cm} and y_{cm} are the x and y components, respectively, of the center-of-mass position $\boldsymbol{r}_{\mathrm{cm}}$. In an elliptical disk elongated along the x axis, the coefficient κ_y is larger than κ_x because of the disk shape anisotropy [33]. Finally, the magnetostatic energy of two vortex state can be expressed as Eq. (6).

IV. RESULTS AND DISCUSSION

A. Solution of the Thiele equation

Equation (3) is solved to obtain the rotational amplitude of each core by assuming that two cores rotate around each equilibrium position [see Eq. (1)]. The detailed calculation is described in the Appendix. The results are as follows:

(i) If $p_1 = +p_2$, then

$$X_{\mathrm{cm}} = \frac{X_1 + X_2}{2} = u_x R_1(\omega_{\mathrm{r}} = \omega_1) + p_1 u_y R_2(\omega_{\mathrm{r}} = \omega_1),$$

$$Y_{\rm cm} = \frac{Y_1 + Y_2}{2} = p_1 u_x R_3(\omega_{\rm r} = \omega_1) + u_y R_4(\omega_{\rm r} = \omega_1),$$
$$X_{\rm rel} = X_2 - X_1 = p_1 h_x R_5(\omega_{\rm r} = \omega_2) + h_y R_6(\omega_{\rm r} = \omega_2),$$
$$Y_{\rm rel} = Y_2 - Y_1 = h_x R_7(\omega_{\rm r} = \omega_2) + p_1 h_y R_8(\omega_{\rm r} = \omega_2). \quad (19)$$

(ii) If $p_1 = -p_2$, then

$$X_{\rm cm} = \frac{X_1 + X_2}{2} = u_x R_9(\omega_{\rm r} = \omega_3) + p_1 h_x R_{10}(\omega_{\rm r} = \omega_3),$$
$$Y_{\rm cm} = \frac{Y_1 + Y_2}{2} = u_y R_{11}(\omega_{\rm r} = \omega_4) + p_1 h_y R_{12}(\omega_{\rm r} = \omega_4),$$
$$X_{\rm rel} = X_2 - X_1 = p_1 u_y R_{13}(\omega_{\rm r} = \omega_4) + h_y R_{14}(\omega_{\rm r} = \omega_4), \quad (20)$$
$$Y_{\rm rel} = Y_2 - Y_1 = p_1 u_x R_{15}(\omega_{\rm r} = \omega_3) + h_x R_{16}(\omega_{\rm r} = \omega_3),$$

where $X_{\rm cm}(Y_{\rm cm})$ and $X_{\rm rel}(Y_{\rm rel})$ correspond to the center-of-mass and relative coordinates of the rotation amplitude $X_j(Y_j)$, respectively. $R_k(\omega_{\rm r})$ consists of a linear combination of the dispersion function and the Lorentzian function with eigenfrequency $\omega_{\rm r}$. The detailed expressions of $R_k(\omega_{\rm r})$ are shown in Eqs. (A18)–(A25) and (A38)–(A45). The resonant frequencies as functions of stiffness constants in Eq. (6) are given by

$$\omega_1 = \sqrt{\frac{\kappa_x \kappa_y}{G_0^2 + \alpha^2 D^2}}, \quad \omega_2 = \sqrt{\frac{\mu^2}{G_0^2 + \alpha^2 D^2}}, \quad (21)$$

$$\omega_3 = \sqrt{\frac{\mu \kappa_x}{G_0^2 + \alpha^2 D^2}}, \quad \omega_4 = \sqrt{\frac{\mu \kappa_y}{G_0^2 + \alpha^2 D^2}}. \quad (22)$$

These resonant frequencies are equivalent to the eigenfrequencies proposed by Buchanan *et al.* [22] although the definition of stiffness constants is different from our analytical model. It is noted that the assumption of harmonic potential given by Eq. (6) enables us to obtain Eqs. (19) and (20), i.e., the dynamic susceptibilities in response to an rf field and an rf spin current.

B. Eigenmodes and eigenfrequencies

1. $p_1 = +p_2$ (two cores with the same polarity)

It can be seen from Eq. (19) that the contribution of the rf spin current, $u_{x(y)}$ only exists in the expressions for $X_{\rm cm}$ and $Y_{\rm cm}$, whereas that of the rf field $h_{x(y)}$ only exists in the expressions for $X_{\rm rel}$ and $Y_{\rm rel}$. The result suggests that the rf spin current excites the center-of-mass motion of the cores whereas the rf field excites the relative motion of cores. The polarity $p_1(=p_2)$ determines direction of rotation: cores rotate clockwise when $p_1 = -1$, and counterclockwise when $p_1 = +1$. At the eigenfrequency, temporal variations of the core displacement calculated from Eqs. (2) and (19) are shown in Figs. 5(a)–5(d). Schematics of these motions are depicted at the top of these figures. The polarities of the vortex pairs are set at $p_1 = p_2 = +1$. Numerical conditions are described in Table I and [34].

The trajectories excited by the rf spin currents along the x and y axes are shown in Figs. 5(a) and 5(b), respectively. It is clearly shown in Figs. 5(a) and 5(b) that rf spin current excites the center-of-mass motion of the cores. Namely, cores gyrate with in-phase (i) mode along both the x and y axes. We define this eigenmode as the (i,i) mode according to Buchanan *et al.* [22]. Note that the first and second parameters of (i,i) indicate that the cores gyrate with an in-phase mode along the x and y axes, respectively. As shown by $X_{\rm cm}$ and $Y_{\rm cm}$ in Eq. (19), the eigenfrequency of the (i,i) mode is given by ω_1.

On the contrary, as shown in Figs. 5(c) and 5(d), the x and y components of the rf magnetic field excite a relative motion of the cores. Namely, the cores gyrate with an out-of-phase (o) mode along both the x and y axes. We define this eigenmode as the (o,o) mode. As shown by $X_{\rm rel}$ and $Y_{\rm rel}$ in Eq. (19), the eigenfrequency of the (o,o) mode is given by ω_2. Note that Figs. 5(a) and 5(b) depict the same rotational mode with different initial phases [and so do Figs. 5(c) and 5(d)]. Thus, it is found that the source of excitation (rf field or rf spin current) decides which eigenmode [(i,i) or (o,o)] will be excited when two cores have the same polarity ($p_1 = +p_2$).

2. $p_1 = -p_2$ (two cores with the opposite polarity)

We consider the contributions from u_x, u_y, h_x, and h_y, separately. As shown in Eq. (20), u_x only exists in the expressions for $X_{\rm cm}$ and $Y_{\rm rel}$. This means that u_x can excite center-of-mass motion in the x direction and relative motion in the y direction simultaneously. At the eigenfrequency, temporal variations of the core displacement are calculated using Eqs. (2) and (20), and are shown in Fig. 5(e). A schematic of the core motion is depicted at the top of Fig. 5(e). The polarities of the vortex pairs are set at $p_1 = -1$ and $p_2 = +1$. One finds that the two cores gyrate in the same phase along the x axis, whereas they gyrate with a phase difference of π along the y axis. The former indicates that cores gyrate with an in-phase (i) mode along the x axis, while the latter indicates that cores gyrate with an out-of-phase (o) mode along the y axis. We define this eigenmode as the (i,o) mode. In the same way, h_x only exists in the expression for $X_{\rm cm}$ and $Y_{\rm rel}$. This means that u_x and h_x excite the same rotational mode [i.e., the (i,o) mode]. Temporal variations of the core displacement excited by h_x are shown in Fig. 5(g). As seen in the expressions for $X_{\rm cm}$ and $Y_{\rm rel}$ in Eq. (20), the eigenfrequency of the (i,o) mode is given by ω_3.

We will now consider the excitation for y direction. First, u_y only exists in the expressions for $X_{\rm rel}$ and $Y_{\rm cm}$ in Eq. (20). This means that u_y can excite relative motion in the x direction and center-of-mass motion in the y direction simultaneously. Temporal variations of the core displacement are shown in Fig. 5(f). One can see that the two cores gyrate with a phase difference of π along the x axis, while they gyrate in the same phase along the y axis. The former indicates that cores gyrate with an out-of-phase (o) mode along the x axis, whereas the latter indicates that cores gyrate with in-phase (i) mode along the y axis. We define this eigenmode as the (o,i) mode. In the same way, h_y only exists in the expressions for $X_{\rm rel}$ and $Y_{\rm cm}$ in Eq. (20). This means that u_y and h_y excite the same rotational mode [the (o,i) mode]. Temporal variation of the core displacement excited by h_y are shown in Fig. 5(h). As seen in the expressions for $X_{\rm rel}$ and $Y_{\rm cm}$ in Eq. (20), the eigenfrequency of the (o,i) mode is given by ω_4. Thus, it is found that the direction of the excitation source (along the x or y axis) decides which eigenmode [the (i,o) mode or the (o,i) mode] is excited when the two cores have the opposite

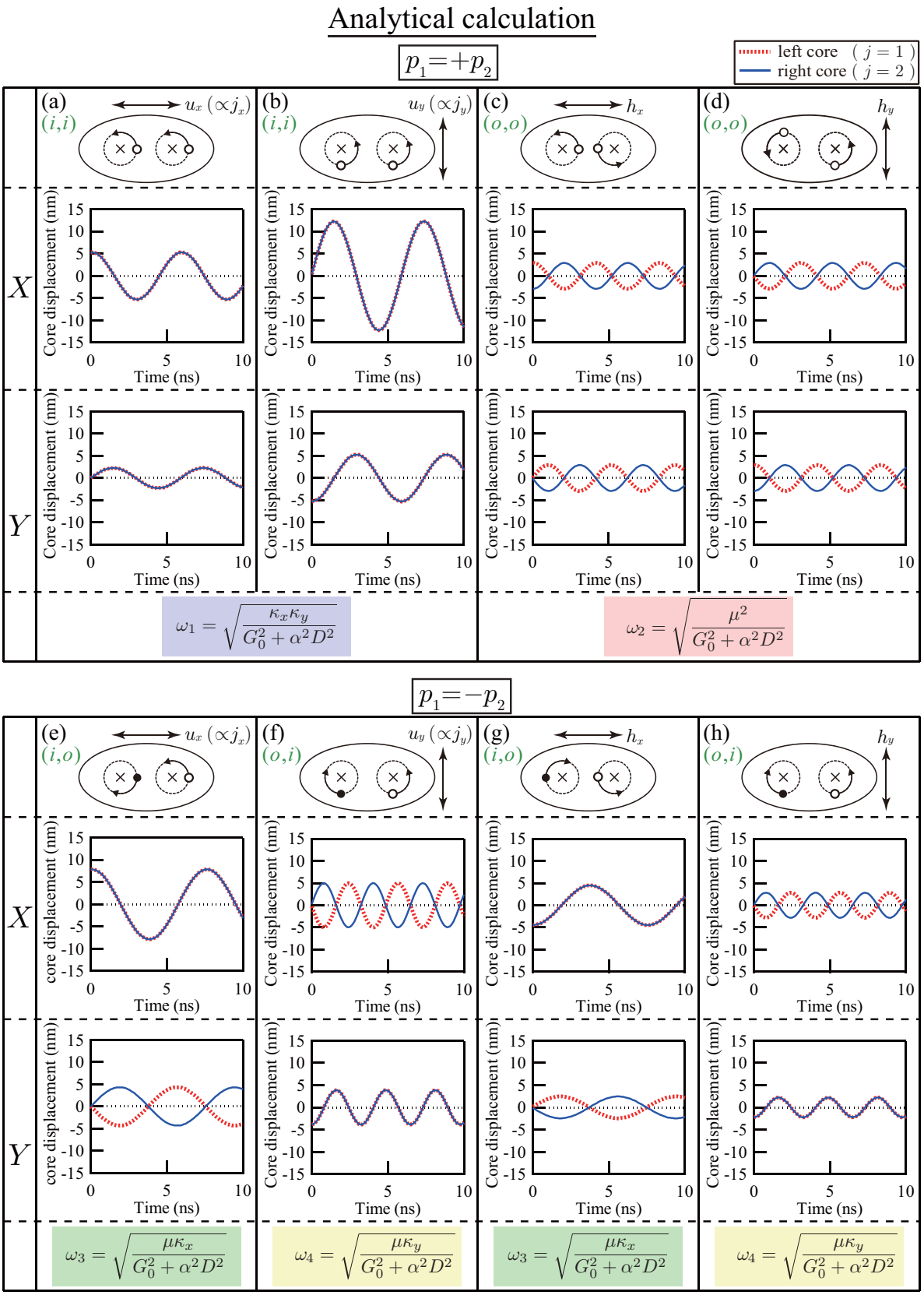

FIG. 5. (Color online) Depictions of the core motions and eigenfrequencies derived by analytical calculation. First row: Schematics of the excitation source and core motions. The open and closed circles represent vortex cores with positive and negative polarity, respectively. "×" marks the center of gyration. Second and third rows: Core displacement along the x and y axes as a function of time. The red dashed line and the blue solid line correspond to the left ($j = 1$) and right ($j = 2$) cores, respectively. Fourth row: Formulas of the eigenfrequencies.

polarity ($p_1 = -p_2$). These results are totally different from the $p_1 = +p_2$ case.

C. Comparison with magnetostatically coupled vortices

In the case where $p_1 = +p_2$, it is found that the source of the excitation (rf field or rf spin current) decides which eigenmode [(i,i) or (o,o)] is excited. As schematically shown in Figs. 5(a)–5(d), the eigenmode is independent of the direction of $\boldsymbol{h}_{\rm ac}$ and $\boldsymbol{j}_{\rm sp}$. The rf spin current excites the (i,i) mode, whose eigenfrequency is ω_1, whereas the rf field excites the (o,o) mode, whose eigenfrequency is ω_2.

On the other hand, in the case of $p_1 = -p_2$, it is found that the direction of the excitation source (along the x or y axis) decides which eigenmode [(i,o) or (o,i)] is excited. Unlike the case where $p_1 = +p_2$, the eigenmode is independent of the excitation source, i.e., $\boldsymbol{h}_{\rm ac}$ and $\boldsymbol{j}_{\rm sp}$. Excitation along the x axis (u_x and h_x) excites the (i,o) mode, whose eigenfrequency is ω_3, while excitation along the y axis (u_y and h_y) excites the (o,i) mode, whose eigenfrequency is ω_4.

In each case, either the center-of-mass motion or the relative motion is excited. We notice that the eigenfrequencies of the center-of-mass motion and the relative motion are different. The eigenfrequency differences of the core motions are similar to those of the two-body problem with springs.

In a previous study, Shibata *et al.* [13] classified the eigenmodes of the vortex pairs in two separate disks. They found that all four eigenmodes [(i,i), (o,o), (i,o), (o,i)] depended on the combination of polarity and chirality. Note that, with separate disks, chirality can take two conditions: $c_1 = +c_2$ and $c_1 = -c_2$. On the other hand, when looking at a pair of vortices confined to the same disk, chirality can take one condition: $c_1 = -c_2$. Buchanan *et al.* [22] found the (o,o), (i,o), and (o,i) modes by rf field excitation under the $c_1 = -c_2$ condition. The (i,i) mode cannot be excited by an rf field. In this study we found the (i,i) mode by rf current excitation in the case of two vortices confined to one disk.

V. MICROMAGNETIC SIMULATION

A. Eigenmodes and eigenfrequencies

To confirm the validity of the analytical calculations discussed in Sec. IV, we carried out a micromagnetic simulation. We used a simulation program based on our originally developed code in this section. Simulation parameters are summarized in Table I, except we neglected the nonadiabaticity parameter, i.e., $\beta = 0$. The simulation cell size was 4 nm × 4 nm × 30 nm. Figure 6 shows the simulated result of temporal variations of the core displacement at the eigenfrequencies for each excitation mode [see Supplemental Material movies (a)–(h) [35]]. Note that the graphs in Fig. 6 show the core movements in the steady state. Movements of the cores were consistent with the analytical result described in Fig. 5. Analytical calculations showed that the eigenmode was selected by the source of excitation, not by the excitation direction, when the two cores have the same polarity ($p_1 = +p_2$). Figures 6(a) and 6(b) show spin current excitations with different excitation directions. The eigenfrequencies of Figs. 6(a) and 6(b) are both 120 MHz, indicating that they excite the same eigenmode. Analytical calculation also showed that the pairs Figs. 6(c) and 6(d), 6(e) and 6(g), and 6(f) and 6(h) each shared an eigenmode. The results of the simulation were consistent with the analytical results.

TABLE III. Eigenfrequencies.

	Analytical calculation	Simulation
f_1	169 MHz	120 MHz
f_2	239 MHz	204 MHz
f_3	132 MHz	96 MHz
f_4	307 MHz	264 MHz

Table III shows comparison of the eigenfrequencies between the analytical calculation and the micromagnetic simulation. One can see that magnitude relationship of $f_1 - f_4$ is consistent between the analytical calculation and the micromagnetic simulation.

B. Distinguishing the peak of the rf spin current from that of the rf field

In experiments, electrodes are often attached to a ferromagnetic disk to study the spin torque effect on a vortex [10,36]. However, rf electric current simultaneously induces an rf Oersed field perpendicular to itself. This rf field makes it difficult to study the spin torque contribution due to the rf current, because the eigenfrequencies of the rf field excitation and the rf spin current excitation are the same in a single vortex state. In a vortex pair, however, the eigenfrequencies of the rf field excitation and of the rf spin current excitation are different whenever they are orthogonally applied. It makes it easy to eliminate the rf field contribution at the eigenfrequency of the spin current excitation. Figure 7(a) shows the gyration radius of the cores as a function of frequency when the rf spin current and the rf field are orthogonally applied at the same time. Two resonance peaks, one excited by the rf spin current and one by the rf field, can be seen in every case. Thus we can distinguish the rf spin current contribution from that of the rf field at each resonance peak. Note that the complex amplitudes caused by the rf-spin-current excitation depend on both α and β, whereas those caused by the rf-field excitation depend only on α [see Eqs. (A18)–(A25) and (A38)–(A45)]. As a consequence, the values of α and β can be individually determined from the two resonance spectra. Figure 7(b) shows the gyration radius of the left core ($j = 1$) as a function of the frequency with various β, when the polarity is $p_1 = +p_2$ and $u_x + h_y$ is applied. Figure 7(c) shows the β dependence of the gyration radius at the eigenfrequencies of the rf spin current excitation (120 MHz) and the rf field excitation (204 MHz). As β increases, the peak height of the spin current excitation increases. On the other hand, the peak height of rf field excitation is independent of β. Thus β can be estimated using the measurement of magnetic vortex pair gyration.

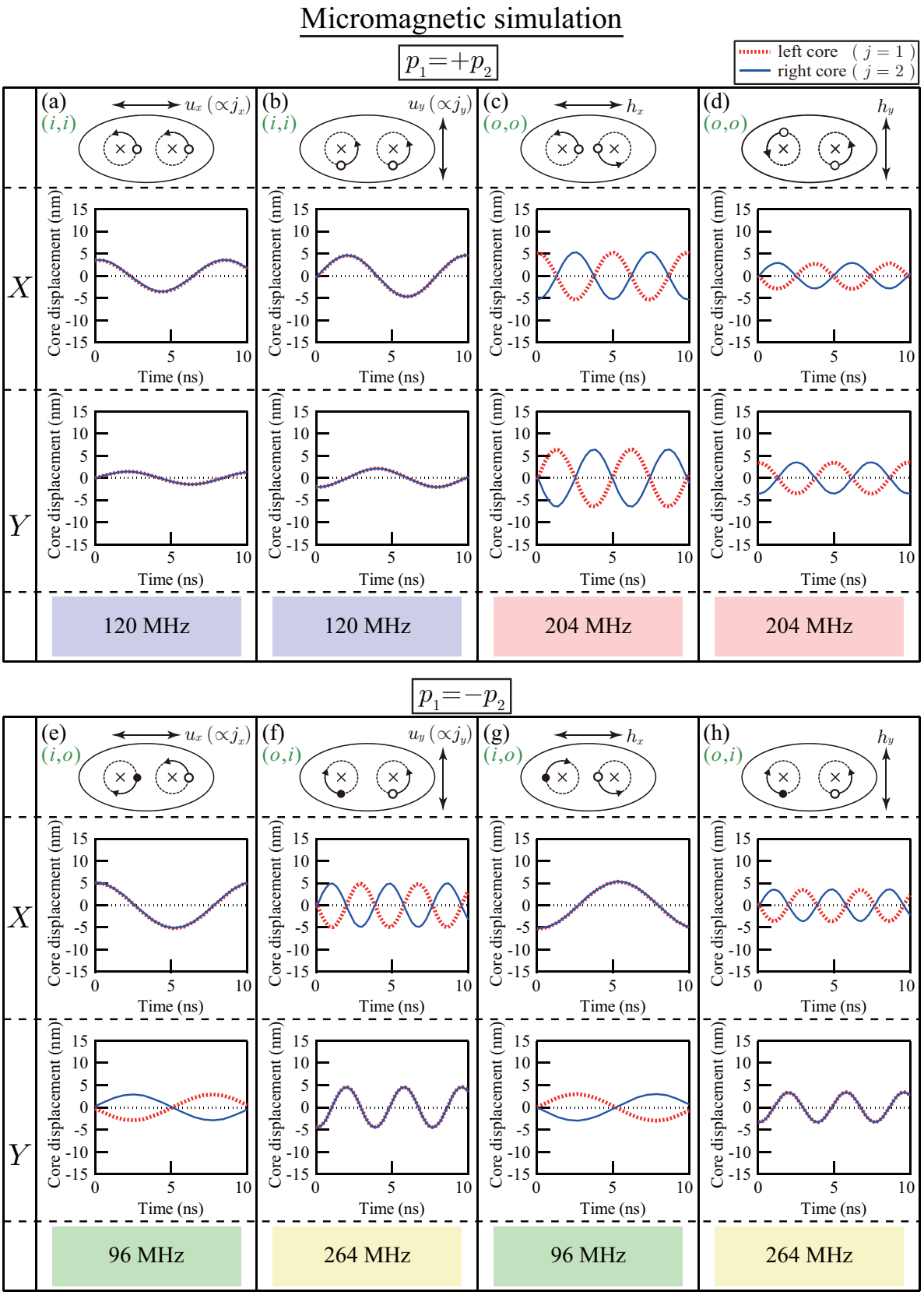

FIG. 6. (Color online) Depictions of the core motions and eigenfrequencies derived from micromagnetic simulation. First row: Schematics of the excitation source and core motions. The open and closed circles represent vortex cores with positive and negative polarity, respectively. "×" marks the center of gyration. Second and third rows: Core displacement along the x and y axes as a function of time. The red dashed line and the blue solid line correspond to the left ($j = 1$) and right ($j = 2$) cores, respectively. Fourth row: Observed eigenfrequencies.

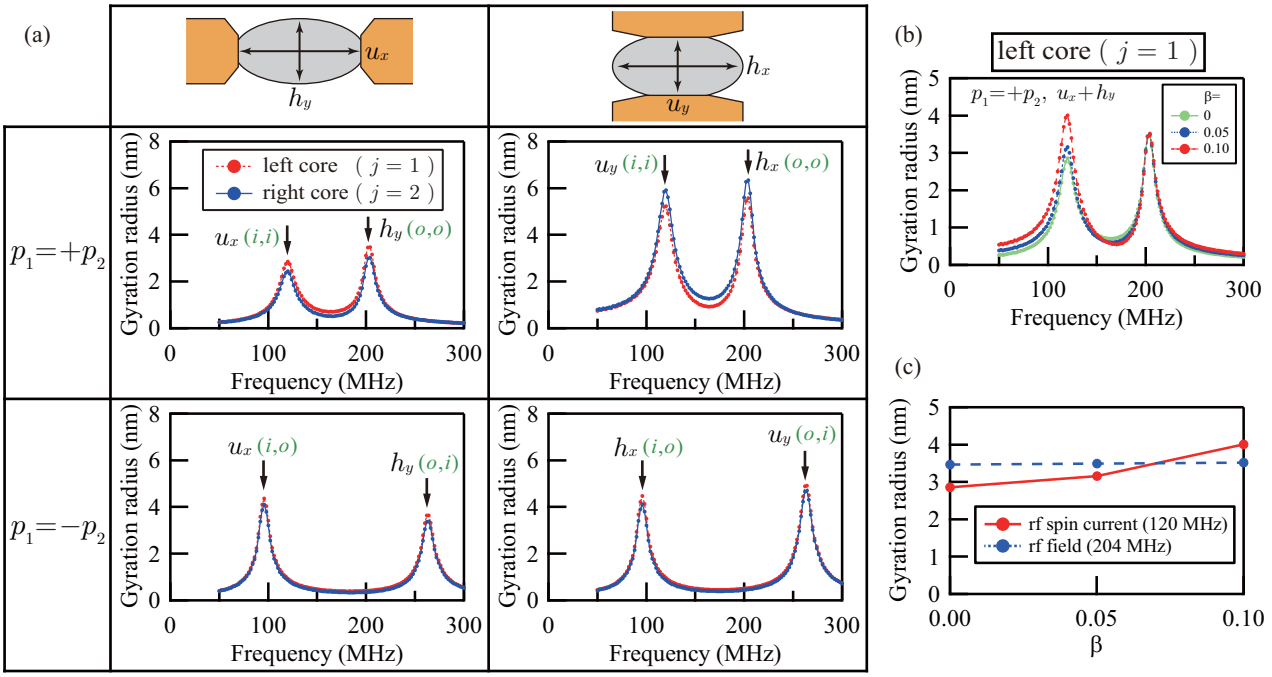

FIG. 7. (Color online) (a) Gyration radius of the cores as a function of the frequency when the rf spin current and the rf field are orthogonally applied at the same time. (b) Gyration radius of the left core ($j = 1$) as a function of the frequency with various β, when the polarity is $p_1 = +p_2$ and $u_x + h_y$ is applied. (c) β dependence of the gyration radius at the eigenfrequency of the rf spin current excitation (red solid line), and that of the rf field excitation (blue dashed line).

VI. CONCLUSION

The motion of a pair of vortex cores confined to a ferromagnetic elliptical disk has been analytically and numerically investigated. By solving the Thiele equation with simultaneous application of the rf magnetic field $\boldsymbol{h}_{\rm rf}$ and the rf spin current $\boldsymbol{j}_{\rm sp}$, the dynamic susceptibility of exchange-coupled vortices in response to $\boldsymbol{h}_{\rm rf}$ and $\boldsymbol{j}_{\rm sp}$ was obtained. It was found that the source of excitation (rf field or rf spin current) decides which eigenmode [(i,i) or (o,o)] is excited when the two cores have the same polarity ($p_1 = +p_2$), whereas the direction of the excitation source (along the x or y axis) decides which eigenmode [(i,o) mode or (o,i) mode] is excited when the two cores have opposite polarity ($p_1 = -p_2$). It is also found that one can obtain two different eigenfrequencies whenever the rf field $\boldsymbol{h}_{\rm rf}$ and the rf spin current $\boldsymbol{j}_{\rm sp}$ are orthogonally applied. This fact can be used to distinguish the rf spin current contribution from the rf field contribution at each resonance peak. Our study sheds light on means to examine an intrinsic material parameter, the nonadiabaticity parameter of STT, β, from extrinsic effects such as an Oersted field.

ACKNOWLEDGMENT

The authors would like to thank K. Hosono and G. Tatara for their valuable discussions.

APPENDIX: ANALYTICAL DERIVATION OF ROTATION AMPLITUDE OF VORTICES

In this section, we solve the Thiele equation to derive the complex amplitude and the eigenfrequency. Equation (3) can be expressed in the matrix form as

$$\begin{aligned}&\begin{pmatrix}\tilde{\alpha} & -p_j\\ p_j & \tilde{\alpha}\end{pmatrix}\begin{pmatrix}\dot{x}_j\\ \dot{y}_j\end{pmatrix}+\begin{pmatrix}\tilde{\kappa}_x & 0\\ 0 & \tilde{\kappa}_y\end{pmatrix}\begin{pmatrix}x_{\rm cm}\\ y_{\rm cm}\end{pmatrix}\\ &\quad+(-1)^j\begin{pmatrix}\tilde{\mu}/2 & 0\\ 0 & \tilde{\mu}/2\end{pmatrix}\begin{pmatrix}x_{\rm rel}-b\\ y_{\rm rel}\end{pmatrix}\\ &=e^{i\omega t}\begin{pmatrix}p_j u_y+\tilde{\beta}u_x+c_j\tilde{l}h_y\\ p_j u_x+\tilde{\beta}u_y-c_j\tilde{l}h_x\end{pmatrix},\end{aligned}\tag{A1}$$

where we introduce the following reduced parameters to simplify the notation:

$$\begin{aligned}&\tilde{\alpha}=\frac{\alpha D}{G_0},\quad \tilde{\beta}=\frac{\beta D}{G_0},\quad \tilde{l}=\frac{l}{G_0},\\ &\tilde{\kappa}_x=\frac{\kappa_x}{G_0},\quad \tilde{\kappa}_y=\frac{\kappa_y}{G_0},\quad \tilde{\mu}=\frac{\mu}{G_0}.\end{aligned}\tag{A2}$$

We assume the vortex position has the following form:

$$\begin{pmatrix}x_1\\ y_1\end{pmatrix}=\begin{pmatrix}-\frac{b}{2}+X_1e^{i\omega t}\\ Y_1e^{i\omega t}\end{pmatrix},\quad \begin{pmatrix}x_2\\ y_2\end{pmatrix}=\begin{pmatrix}\frac{b}{2}+X_2e^{i\omega t}\\ Y_2e^{i\omega t}\end{pmatrix},\tag{A3}$$

where X_j and Y_j are the complex amplitudes. Substituting Eq. (A3) into Eq. (A1), we obtain

$$\begin{aligned}&\begin{pmatrix}i\omega\tilde{\alpha} & -i\omega p_j\\ i\omega p_j & i\omega\tilde{\alpha}\end{pmatrix}\begin{pmatrix}X_j\\ Y_j\end{pmatrix}+\begin{pmatrix}\tilde{\kappa}_x & 0\\ 0 & \tilde{\kappa}_y\end{pmatrix}\begin{pmatrix}X_{\rm cm}\\ Y_{\rm cm}\end{pmatrix}\\ &+(-1)^j\begin{pmatrix}\tilde{\mu}/2 & 0\\ 0 & \tilde{\mu}/2\end{pmatrix}\begin{pmatrix}X_{\rm rel}\\ Y_{\rm rel}\end{pmatrix}=\begin{pmatrix}p_j u_y+\tilde{\beta}u_x+c_j\tilde{l}h_y\\ p_j u_x+\tilde{\beta}u_y-c_j\tilde{l}h_x\end{pmatrix},\end{aligned}\tag{A4}$$

where

$$\begin{pmatrix} X_{\rm cm} \\ Y_{\rm cm} \end{pmatrix} = \begin{pmatrix} (X_1+X_2)/2 \\ (Y_1+Y_2)/2 \end{pmatrix}, \quad \begin{pmatrix} X_{\rm rel} \\ Y_{\rm rel} \end{pmatrix} = \begin{pmatrix} X_2-X_1 \\ Y_2-Y_1 \end{pmatrix}. \tag{A5}$$

Equation (A4) leads to the following equations:

(i) If $p_1 = +p_2$:

$$\begin{pmatrix} i\omega\tilde{\alpha}+\tilde{\kappa}_x & -i\omega p_1 \\ i\omega p_1 & i\omega\tilde{\alpha}+\tilde{\kappa}_y \end{pmatrix}\begin{pmatrix} X_{\rm cm} \\ Y_{\rm cm} \end{pmatrix} = \begin{pmatrix} p_1u_y+\tilde{\beta}u_x \\ p_1u_x+\tilde{\beta}u_y \end{pmatrix}, \tag{A6}$$

$$\begin{pmatrix} i\omega\tilde{\alpha}+\tilde{\mu} & -i\omega p_1 \\ i\omega p_1 & i\omega\tilde{\alpha}+\tilde{\mu} \end{pmatrix}\begin{pmatrix} X_{\rm rel} \\ Y_{\rm rel} \end{pmatrix} = 2c_1\tilde{l}\begin{pmatrix} -h_y \\ h_x \end{pmatrix}. \tag{A7}$$

(ii) If $p_1 = -p_2$:

$$\begin{pmatrix} i\omega\tilde{\alpha}+\tilde{\kappa}_x & 0 \\ 0 & i\omega\tilde{\alpha}+\tilde{\kappa}_y \end{pmatrix}\begin{pmatrix} X_{\rm cm} \\ Y_{\rm cm} \end{pmatrix} + \begin{pmatrix} 0 & i\omega p_1/2 \\ -i\omega p_1/2 & 0 \end{pmatrix}\begin{pmatrix} X_{\rm rel} \\ Y_{\rm rel} \end{pmatrix} = \begin{pmatrix} \tilde{\beta}u_x \\ \tilde{\beta}u_y \end{pmatrix}, \tag{A8}$$

$$\begin{pmatrix} 0 & -i\omega p_1 \\ i\omega p_1 & 0 \end{pmatrix}\begin{pmatrix} X_{\rm cm} \\ Y_{\rm cm} \end{pmatrix} + \begin{pmatrix} -(i\omega\tilde{\alpha}+\tilde{\mu})/2 & 0 \\ 0 & -(i\omega\tilde{\alpha}+\tilde{\mu})/2 \end{pmatrix}\begin{pmatrix} X_{\rm rel} \\ Y_{\rm rel} \end{pmatrix} = \begin{pmatrix} p_1u_y+c_1\tilde{l}h_y \\ p_1u_x-c_1\tilde{l}h_x \end{pmatrix}. \tag{A9}$$

Here, we used $c_2 = -c_1$. In the case of $p_1 = +p_2$, the center-of-mass motion only depends on $\boldsymbol{u}$, and the relative motion only depends on $\boldsymbol{h}$, as can be seen in Eqs. (A6) and (A7). On the other hand, in the case of $p_1 = -p_2$, the center-of-mass motion and the relative motion depend on both $\boldsymbol{u}$ and $\boldsymbol{h}$, as can be seen in Eqs. (A8) and (A9). Therefore, we derive the eigenmodes of the two vortices for the former and the latter cases separately. In Appendix 1, we show the case of $p_1 = +p_2$. In Appendix 2, we show the case of $p_1 = -p_2$.

1. $p_1 = +p_2$ (two cores with same polarity)

The inverse matrix of the coefficient matrix on the left-hand side of Eqs. (A6) and (A7) can be calculated as

$$\begin{pmatrix} i\omega\tilde{\alpha}+\tilde{\kappa}_x & -i\omega p_1 \\ i\omega p_1 & i\omega\tilde{\alpha}+\tilde{\kappa}_y \end{pmatrix}^{-1} = \frac{(\omega_1^2-\omega^2)-i\omega\alpha_1}{(1+\tilde{\alpha}^2)\left[\left(\omega_1^2-\omega^2\right)^2+(\omega\alpha_1)^2\right]}\begin{pmatrix} i\omega\tilde{\alpha}+\tilde{\kappa}_y & i\omega p_1 \\ -i\omega p_1 & i\omega\tilde{\alpha}+\tilde{\kappa}_x \end{pmatrix}, \tag{A10}$$

$$\begin{pmatrix} i\omega\tilde{\alpha}+\tilde{\mu} & -i\omega p_1 \\ i\omega p_1 & i\omega\tilde{\alpha}+\tilde{\mu} \end{pmatrix}^{-1} = \frac{(\omega_2^2-\omega^2)-i\omega\alpha_2}{(1+\tilde{\alpha}^2)\left[\left(\omega_2^2-\omega^2\right)^2+(\omega\alpha_2)^2\right]}\begin{pmatrix} i\omega\tilde{\alpha}+\tilde{\mu} & i\omega p_1 \\ -i\omega p_1 & i\omega\tilde{\alpha}+\tilde{\mu} \end{pmatrix}, \tag{A11}$$

where

$$\alpha_1 = \frac{\tilde{\alpha}(\tilde{\kappa}_x+\tilde{\kappa}_y)}{1+\tilde{\alpha}^2}, \quad \omega_1 = \sqrt{\frac{\tilde{\kappa}_x\tilde{\kappa}_y}{1+\tilde{\alpha}^2}} = \sqrt{\frac{\kappa_x\kappa_y}{G_0^2+\alpha^2D^2}}, \tag{A12}$$

$$\alpha_2 = \frac{2\tilde{\alpha}\tilde{\mu}}{1+\tilde{\alpha}^2}, \quad \omega_2 = \sqrt{\frac{\tilde{\mu}^2}{1+\tilde{\alpha}^2}} = \sqrt{\frac{\mu^2}{G_0^2+\alpha^2D^2}}. \tag{A13}$$

Using these inverse matrices, Eqs. (A6) and (A7) lead to the following:

$$X_{\rm cm} = u_xR_1(\omega_{\rm r}=\omega_1) + p_1u_yR_2(\omega_{\rm r}=\omega_1), \tag{A14}$$

$$Y_{\rm cm} = p_1u_xR_3(\omega_{\rm r}=\omega_1) + u_yR_4(\omega_{\rm r}=\omega_1), \tag{A15}$$

$$X_{\rm rel} = p_1h_xR_5(\omega_{\rm r}=\omega_2) + h_yR_6(\omega_{\rm r}=\omega_2), \tag{A16}$$

$$Y_{\rm rel} = h_xR_7(\omega_{\rm r}=\omega_2) + p_1h_yR_8(\omega_{\rm r}=\omega_2), \tag{A17}$$

where

$$R_1(\omega_{\rm r}=\omega_1) = \frac{\left[\tilde{\beta}\tilde{\kappa}_y\left(\omega_1^2-\omega^2\right)+\alpha_1\omega^2(1+\tilde{\alpha}\tilde{\beta})\right]+i\omega\left[(1+\tilde{\alpha}\tilde{\beta})\left(\omega_1^2-\omega^2\right)-\alpha_1\tilde{\beta}\tilde{\kappa}_y\right]}{(1+\tilde{\alpha}^2)\left[\left(\omega_1^2-\omega^2\right)^2+(\omega\alpha_1)^2\right]}, \tag{A18}$$

$$R_2(\omega_{\rm r}=\omega_1) = \frac{\left[\tilde{\kappa}_y\left(\omega_1^2-\omega^2\right)+\alpha_1\omega^2(\tilde{\alpha}+\tilde{\beta})\right]+i\omega\left[(\tilde{\alpha}+\tilde{\beta})\left(\omega_1^2-\omega^2\right)-\alpha_1\tilde{\kappa}_y\right]}{(1+\tilde{\alpha}^2)\left[\left(\omega_1^2-\omega^2\right)^2+(\omega\alpha_1)^2\right]}, \tag{A19}$$

$$R_3(\omega_{\rm r}=\omega_1) = \frac{\left[\tilde{\kappa}_x\left(\omega_1^2-\omega^2\right)+\alpha_1\omega^2(\tilde{\alpha}-\tilde{\beta})\right]+i\omega\left[(\tilde{\alpha}-\tilde{\beta})\left(\omega_1^2-\omega^2\right)-\alpha_1\tilde{\kappa}_x\right]}{(1+\tilde{\alpha}^2)\left[\left(\omega_1^2-\omega^2\right)^2+(\omega\alpha_1)^2\right]}, \tag{A20}$$

$$R_4(\omega_{\rm r}=\omega_1) = \frac{\left[\tilde{\beta}\tilde{\kappa}_x\left(\omega_1^2-\omega^2\right)+\alpha_1\omega^2(\tilde{\alpha}\tilde{\beta}-1)\right]+i\omega\left[(\tilde{\alpha}\tilde{\beta}-1)\left(\omega_1^2-\omega^2\right)-\alpha_1\tilde{\beta}\tilde{\kappa}_x\right]}{(1+\tilde{\alpha}^2)\left[\left(\omega_1^2-\omega^2\right)^2+(\omega\alpha_1)^2\right]}, \tag{A21}$$

$$R_5(\omega_r=\omega_2)=2c_1\tilde{l}\frac{\alpha_2\omega^2+i\omega\left(\omega_2^2-\omega^2\right)}{(1+\tilde{\alpha}^2)\left[\left(\omega_2^2-\omega^2\right)^2+(\omega\alpha_2)^2\right]}, \tag{A22}$$

$$R_6(\omega_r=\omega_2)=-2c_1\tilde{l}\frac{\left[\tilde{\mu}\left(\omega_2^2-\omega^2\right)+\alpha_2\tilde{\alpha}\omega^2\right]+i\omega\left[\tilde{\alpha}\left(\omega_2^2-\omega^2\right)-\alpha_2\tilde{\mu}\right]}{(1+\tilde{\alpha}^2)\left[\left(\omega_2^2-\omega^2\right)^2+(\omega\alpha_2)^2\right]}, \tag{A23}$$

$$R_7(\omega_r=\omega_2)=2c_1\tilde{l}\frac{\left[\tilde{\mu}\left(\omega_2^2-\omega^2\right)+\alpha_2\tilde{\alpha}\omega^2\right]+i\omega\left[\tilde{\alpha}\left(\omega_2^2-\omega^2\right)-\alpha_2\tilde{\mu}\right]}{(1+\tilde{\alpha}^2)\left[\left(\omega_2^2-\omega^2\right)^2+(\omega\alpha_2)^2\right]}, \tag{A24}$$

$$R_8(\omega_r=\omega_2)=2c_1\tilde{l}\frac{\alpha_2\omega^2+i\omega\left(\omega_2^2-\omega^2\right)}{(1+\tilde{\alpha}^2)\left[\left(\omega_2^2-\omega^2\right)^2+(\omega\alpha_2)^2\right]}. \tag{A25}$$

These equations consist of the dispersion functions and Lorentzian functions with the eigenfrequencies ω_1 or ω_2.

2. $p_1=-p_2$ (two cores have the opposite polarity)

Equations (A8) and (A9) can be simply expressed as

$$\begin{pmatrix}A & 0\\ 0 & B\end{pmatrix}\begin{pmatrix}X_{cm}\\ Y_{cm}\end{pmatrix}+\begin{pmatrix}0 & C/2\\ -C/2 & 0\end{pmatrix}\begin{pmatrix}X_{rel}\\ Y_{rel}\end{pmatrix}=\begin{pmatrix}E\\ F\end{pmatrix}, \tag{A26}$$

$$\begin{pmatrix}0 & -C\\ C & 0\end{pmatrix}\begin{pmatrix}X_{cm}\\ Y_{cm}\end{pmatrix}+\begin{pmatrix}-G/2 & 0\\ 0 & -G/2\end{pmatrix}\begin{pmatrix}X_{rel}\\ Y_{rel}\end{pmatrix}=\begin{pmatrix}H\\ I\end{pmatrix}, \tag{A27}$$

where

$$A=i\omega\tilde{\alpha}+\tilde{\kappa}_x,\quad B=i\omega\tilde{\alpha}+\tilde{\kappa}_y,\quad C=i\omega p_1,\quad E=\tilde{\beta}u_x,\quad F=\tilde{\beta}u_y,\quad G=i\omega\tilde{\alpha}+\tilde{\mu},\quad H=p_1u_y+c_1\tilde{l}h_y,\quad I=p_1u_x-c_1\tilde{l}h_x. \tag{A28}$$

Equations (A26) and (A27) lead to

$$X_{cm}=\frac{CI+EG}{AG+C^2},\quad Y_{cm}=\frac{FG-CH}{BG+C^2},\quad X_{rel}=-2\frac{BH+CF}{BG+C^2},\quad Y_{rel}=2\frac{CE-AI}{AG+C^2}. \tag{A29}$$

The denominators in Eq. (A29) can be calculated as

$$\frac{1}{AG+C^2}=\frac{\left(\omega_3^2-\omega^2\right)-i\omega\alpha_3}{(1+\tilde{\alpha}^2)\left[\left(\omega_3^2-\omega^2\right)^2+(\omega\alpha_3)^2\right]}, \tag{A30}$$

$$\frac{1}{BG+C^2}=\frac{\left(\omega_4^2-\omega^2\right)-i\omega\alpha_4}{(1+\tilde{\alpha}^2)\left[\left(\omega_4^2-\omega^2\right)^2+(\omega\alpha_4)^2\right]}, \tag{A31}$$

where

$$\alpha_3=\frac{\tilde{\alpha}(\tilde{\mu}+\tilde{\kappa}_x)}{1+\tilde{\alpha}^2},\quad \omega_3=\sqrt{\frac{\tilde{\mu}\tilde{\kappa}_x}{1+\tilde{\alpha}^2}}=\sqrt{\frac{\mu\kappa_x}{G_0^2+\alpha^2D^2}}, \tag{A32}$$

$$\alpha_4=\frac{\tilde{\alpha}(\tilde{\mu}+\tilde{\kappa}_y)}{1+\tilde{\alpha}^2},\quad \omega_4=\sqrt{\frac{\tilde{\mu}\tilde{\kappa}_y}{1+\tilde{\alpha}^2}}=\sqrt{\frac{\mu\kappa_y}{G_0^2+\alpha^2D^2}}. \tag{A33}$$

Using Eqs. (A30) and (A31), Eqs. (A29) leads to the following:

$$X_{cm}=u_xR_9(\omega_r=\omega_3)+p_1h_xR_{10}(\omega_r=\omega_3), \tag{A34}$$

$$Y_{cm}=u_yR_{11}(\omega_r=\omega_4)+p_1h_yR_{12}(\omega_r=\omega_4), \tag{A35}$$

$$X_{rel}=p_1u_yR_{13}(\omega_r=\omega_4)+h_yR_{14}(\omega_r=\omega_4), \tag{A36}$$

$$Y_{rel}=p_1u_xR_{15}(\omega_r=\omega_3)+h_xR_{16}(\omega_r=\omega_3), \tag{A37}$$

where

$$R_9(\omega_r=\omega_3)=\frac{\left[\tilde{\beta}\tilde{\mu}\left(\omega_3^2-\omega^2\right)+\alpha_3\omega^2(1+\tilde{\alpha}\tilde{\beta})\right]+i\omega\left[(1+\tilde{\alpha}\tilde{\beta})\left(\omega_3^2-\omega^2\right)-\alpha_3\tilde{\beta}\tilde{\mu}\right]}{(1+\tilde{\alpha}^2)\left[\left(\omega_3^2-\omega^2\right)^2+(\omega\alpha_3)^2\right]}, \tag{A38}$$

$$R_{10}(\omega_r=\omega_3)=-c_1\tilde{l}\frac{\alpha_3\omega^2+i\omega\left(\omega_3^2-\omega^2\right)}{(1+\tilde{\alpha}^2)\left[\left(\omega_3^2-\omega^2\right)^2+(\omega\alpha_3)^2\right]}, \tag{A39}$$

$$R_{11}(\omega_r=\omega_4)=\frac{\left[\tilde{\beta}\tilde{\mu}\left(\omega_4^2-\omega^2\right)+\alpha_4\omega^2(\tilde{\alpha}\tilde{\beta}-1)\right]+i\omega\left[(\tilde{\alpha}\tilde{\beta}-1)\left(\omega_4^2-\omega^2\right)-\alpha_4\tilde{\beta}\tilde{\mu}\right]}{(1+\tilde{\alpha}^2)\left[\left(\omega_4^2-\omega^2\right)^2+(\omega\alpha_4)^2\right]}, \tag{A40}$$

$$R_{12}(\omega_r=\omega_4)=-c_1\tilde{l}\frac{\alpha_4\omega^2+i\omega\left(\omega_4^2-\omega^2\right)}{(1+\tilde{\alpha}^2)\left[\left(\omega_4^2-\omega^2\right)^2+(\omega\alpha_4)^2\right]}, \tag{A41}$$

$$R_{13}(\omega_r=\omega_4)=-2\frac{\left[\tilde{\kappa}_y\left(\omega_4^2-\omega^2\right)+\alpha_4\omega^2(\tilde{\alpha}+\tilde{\beta})\right]+i\omega\left[(\tilde{\alpha}+\tilde{\beta})\left(\omega_4^2-\omega^2\right)-\alpha_4\tilde{\kappa}_y\right]}{(1+\tilde{\alpha}^2)\left[\left(\omega_4^2-\omega^2\right)^2+(\omega\alpha_4)^2\right]}, \tag{A42}$$

$$R_{14}(\omega_r=\omega_4)=-2c_1\tilde{l}\frac{\left[\tilde{\kappa}_y\left(\omega_4^2-\omega^2\right)+\alpha_4\tilde{\alpha}\omega^2\right]+i\omega\left[\tilde{\alpha}\left(\omega_4^2-\omega^2\right)-\alpha_4\tilde{\kappa}_y\right]}{(1+\tilde{\alpha}^2)\left[\left(\omega_4^2-\omega^2\right)^2+(\omega\alpha_4)^2\right]}, \tag{A43}$$

$$R_{15}(\omega_r=\omega_3)=-2\frac{\left[\tilde{\kappa}_x\left(\omega_3^2-\omega^2\right)+\alpha_3\omega^2(\tilde{\alpha}-\tilde{\beta})\right]+i\omega\left[(\tilde{\alpha}-\tilde{\beta})\left(\omega_3^2-\omega^2\right)-\alpha_3\tilde{\kappa}_x\right]}{(1+\tilde{\alpha}^2)\left[\left(\omega_3^2-\omega^2\right)^2+(\omega\alpha_3)^2\right]}, \tag{A44}$$

$$R_{16}(\omega_r=\omega_3)=2c_1\tilde{l}\frac{\left[\tilde{\kappa}_x\left(\omega_3^2-\omega^2\right)+\alpha_3\tilde{\alpha}\omega^2\right]+i\omega\left[\tilde{\alpha}\left(\omega_3^2-\omega^2\right)-\alpha_3\tilde{\kappa}_x\right]}{(1+\tilde{\alpha}^2)\left[\left(\omega_3^2-\omega^2\right)^2+(\omega\alpha_3)^2\right]}. \tag{A45}$$

[1] S. Bohlens, B. Krüger, A. Drews, M. Bolte, G. Meier, and D. Pfannkuche, Appl. Phys. Lett. **93**, 142508 (2008).
[2] K. Yamada, S. Kasai, Y. Nakatani, K. Kobayashi, H. Kohno, A. Thiaville, and T. Ono, Nat. Mater. **6**, 270 (2007).
[3] K. Nakano, D. Chiba, N. Ohshima, S. Kasai, T. Sato, Y. Nakatani, K. Sekiguchi, K. Kobayashi, and T. Ono, Appl. Phys. Lett. **99**, 262505 (2011).
[4] J. C. Slonczewski, J. Magn. Magn. Mater. **159**, L1 (1996).
[5] A. Yamaguchi, T. Ono, S. Nasu, K. Miyake, K. Mibu, and T. Shinjo, Phys. Rev. Lett. **92**, 077205 (2004).
[6] Z. Li and S. Zhang, Phys. Rev. B **70**, 024417 (2004).
[7] S. Zhang and Z. Li, Phys. Rev. Lett. **93**, 127204 (2004).
[8] B. Krüger, A. Drews, M. Bolte, U. Merkt, D. Pfannkuche, and G. Meier, Phys. Rev. B **76**, 224426 (2007).
[9] M. Bolte, G. Meier, B. Krüger, A. Drews, R. Eiselt, L. Bocklage, S. Bohlens, T. Tyliszczak, A. Vansteenkiste, B. Van Waeyenberge, K. W. Chou, A. Puzic, and H. Stoll, Phys. Rev. Lett. **100**, 176601 (2008).
[10] M. Goto, H. Hata, A. Yamaguchi, Y. Nakatani, T. Yamaoka, Y. Nozaki, and H. Miyajima, Phys. Rev. B **84**, 064406 (2011).
[11] T. Shinjo, T. Okuno, R. Hassdorf, K. Shigeto, and T. Ono, Science **289**, 930 (2000).
[12] A. Wachowiak, J. Wiebe, M. Bode, O. Pietzsch, M. Morgenstern, and R. Wiesendanger, Science **298**, 577 (2002).
[13] J. Shibata, K. Shigeto, and Y. Otani, Phys. Rev. B **67**, 224404 (2003).
[14] O. V. Sukhostavets, J. M. Gonzalez, and K. Y. Guslienko, Appl. Phys. Exp. **4**, 065003 (2011).
[15] H. Jung, K.-S. Lee, D.-E. Jeong, Y.-S. Choi, Y.-S. Yu, D.-S. Han, A. Vogel, L. Bocklage, G. Meier, M.-Y. Im, P. Fischer, and S.-K. Kim, Sci. Rep. **1**, 59 (2011).
[16] S. Sugimoto, Y. Fukuma, and Y. Otani, IEEE Trans. Magn. **47**, 2951 (2011).
[17] A. Vogel, A. Drews, T. Kamionka, M. Bolte, and G. Meier, Phys. Rev. Lett. **105**, 037201 (2010).
[18] A. A. Awad, G. R. Aranda, D. Dieleman, K. Y. Guslienko, G. N. Kakazei, B. A. Ivanov, and F. G. Aliev, Appl. Phys. Lett. **97**, 132501 (2010).
[19] A. Barman, S. Barman, T. Kimura, Y. Fukuma, and Y. Otani, J. Phys. D **43**, 422001 (2010).
[20] S. S. Cherepov, B. C. Koop, A. Yu. Galkin, R. S. Khymyn, B. A. Ivanov, D. C. Worledge, and V. Korenivski, Phys. Rev. Lett. **109**, 097204 (2012).
[21] K. Y. Guslienko, K. S. Buchanan, S. D. Bader, and V. Novosad, Appl. Phys. Lett. **86**, 223112 (2005).
[22] K. S. Buchanan, P. E. Roy, M. Grimsditch, F. Y. Fradin, K. Y. Guslienko, S. D. Bader, and V. Novosad, Nat. Phys. **1**, 172 (2005).
[23] S. Jain, H. Schultheiss, O. Heinonen, F. Y. Fradin, J. E. Pearson, S. D. Bader, and V. Novosad, Phys. Rev. B **86**, 214418 (2012).
[24] A. A. Thiele, Phys. Rev. Lett. **30**, 230 (1973).
[25] D. L. Huber, J. Appl. Phys. **53**, 1899 (1982).
[26] J. Shibata, Y. Nakatani, G. Tatara, H. Kohno, and Y. Otani, Phys. Rev. B **73**, 020403 (2006).
[27] B. A. Ivanov and C. E. Zaspel, Phys. Rev. Lett. **99**, 247208 (2007).

[28] R. Moriya, L. Thomas, M. Hayashi, Y. B. Bazaliy, C. Rettner, and S. S. P. Parkin, Nat. Phys. **4**, 368 (2008).

[29] V. S. Pribiag, I. N. Krivorotov, G. D. Fuchs, P. M. Braganca, O. Ozatay, J. C. Sankey, D. C. Ralph, and R. A. Buhrman, Nat. Phys. **3**, 498 (2007).

[30] K. Y. Guslienko, Appl. Phys. Lett. **89**, 022510 (2006).

[31] At $\theta = 44.7^\circ$, $b = 1.00\ \mu$m and $r_x = 1.01\ \mu$m are obtained, meaning that the core displacement from its equilibrium position was 5 nm, which is much shorter than the disk size.

[32] OOMMF User's Guide, Version 1.0, M. J. Donahue and D. G. Porter, Interagency Report No. NISTIR 6376, National Institute of Standards and Technology, Gaithersburg, MD, 1999, http://math.nist.gov/oommf/

[33] K. S. Buchanan, P. E. Roy, M. Grimsditch, F. Y. Fradin, K. Y. Guslienko, S. D. Bader, and V. Novosad, Phys. Rev. B **74**, 064404 (2006).

[34] When deriving the graphs in Fig. 5, the following parameters were calculated: $G_0 = 8.57 \times 10^{-13}$ kg/s, $D/G_0 = 3.30$, $\tilde{\alpha} = \tilde{\beta} = 0.033$, $u_{x,y} = 0.51$ m/s, $\tilde{l}h_{x,y} = 0.29$ m/s. The spring constant for relative motion was $\mu = 1.29 \times 10^{-3}$ J/m^2, using the analytical result. The spring constants for center-of-mass motion were estimated to be $\kappa_x = 3.92 \times 10^{-4}$ J/m^2 and $\kappa_y = 2.12 \times 10^{-3}$ J/m^2, which are the simulation results for a single vortex core with the same disk size. These parameters lead to $\tilde{\mu} = 1.51 \times 10^9$ s^{-1}, $\tilde{\kappa}_x = 4.58 \times 10^8$ s^{-1}, and $\tilde{\kappa}_y = 2.47 \times 10^9$ s^{-1}. The polarity was $p_1 = p_2 = +1$ ($p_1 = +p_2$ case) or $p_1 = -1$, $p_2 = +1$ ($p_1 = -p_2$ case). The chirality was $c_1 = -1, c_2 = +1$.

[35] See Supplemental Material at http://link.aps.org/supplemental/10.1103/PhysRevB.90.104418 for movies of core motions at the eigenfrequencies for each excitation mode.

[36] S. Kasai, P. Fischer, M.-Y. Im, K. Yamada, Y. Nakatani, K. Kobayashi, H. Kohno, and T. Ono, Phys. Rev. Lett. **101**, 237203 (2008).